The International Journal of Advanced Manufacturing Technology (2024) 133:2363–2380
https://doi.org/10.1007/s00170-024-13797-0

ORIGINAL ARTICLE

Analytical and FEM models for thermal analysis and residual stresses using wire arc-based welding and additive manufacturing of SUS304

Muhammad Arif Mahmood[1] · Usman Tariq[2] · Mihai Oane[3] · Frank Liou[2]

Received: 1 December 2023 / Accepted: 21 May 2024 / Published online: 8 June 2024

Abstract

Austenitic stainless steel, also known as SUS304, has a wide industrial application. The resultant residual stresses and deformation due to arc welding play a critical role in an in-service SUS04 part failure. Various experimental studies have been presented to predict residual stresses and part deformation. However, these techniques are expensive and time-consuming owing to the trial-and-error approach, limiting their application to industrial applications. Based on the emergent need, this study introduces two simulation models based on analytical and FEM techniques for thermal distribution and residual stress estimation. The experimentally calibrated models results have been implemented for SUS304 multi-pass arc welding. For the analytical simulation framework, a thermal model by considering the arc torch energy attenuation has been solved and provided as an input to the residual stress distribution model solved using Green's function technique. For FEM, a thermo-mechanical coupled model has been proposed and solved using the symmetrical technique. A close correlation has been identified among the analytical, FEM, and experimental techniques. It was found that during the second welding pass, a significant increase in the peak temperature was observed due to elevated arc-material interaction, leading to an expanded heat-affected zone and melt pool. Residual stress analysis highlighted the crucial role of thermal gradient and cooling mechanisms in generating stress within the weld region, which is essential for material strength assessment and failure prediction. This study offers a comprehensive understanding of the thermal and residual stress behaviors in multi-pass arc welding of SUS304 stainless steel bulk plates and can be applied to arc-based additive manufacturing processes.

Keywords Multi-pass arc welding · Residual stresses · Austenitic stainless steel SUS304 · FEM analysis · Analytical framework

1 Introduction

Austenitic stainless steel, also known as SUS304, is extensively utilized to produce nuclear reactors, the medical field, food, and dyeing equipment [1–3]. Its broad use is supported by impressive mechanical qualities and exceptional corrosion resistance [4–6]. These structures invariably necessitate integration with other components through welding techniques to enable multi-functional capabilities [7–9]. However, the welding of SUS304 brings with it a propensity for post-welding defects [10–12]. Given the severe influence of these imperfections on the mechanical characteristics of SUS304 components, the removal of welding errors is critical to ensure the strength of the welded components [13, 14]. In terms of cost-effectiveness, the deployment of welding, particularly for repair, requires the complete resolution of weld-related defects [15, 16].

The inevitability of residual stresses (RS) along with the deformation emerges during the welding process due to localized fast heating and subsequent cooling in the welded region and its immediate surroundings [17–19]. Notably, the welded region is usually very small compared to the bulk plates, imposing more limits on the filler metal within this welded zone by the adjacent material [20–22]. As a result, RS after welding cool-down is typically greater compared to those created at the start of welding. Notably, increased

✉ Muhammad Arif Mahmood
mmahmood@mst.edu

[1] Intelligent Systems Center, Missouri University of Science and Technology, Rolla, MO 65409, USA

[2] Department of Mechanical and Aerospace Engineering, Missouri University of Science and Technology, Rolla, MO 65409, USA

[3] National Institute for Laser, Plasma and Radiation Physics (INFLPR), Ilfov, Magurele 077125, Romania

tensile stress plays an important role because it can cause stress corrosion cracking (SCC), a condition that drastically reduces the lifespan of these structures [23–25]. To reduce SCC susceptibility, it is critical to analyze the amplitude and spatial scattering of RS inside welded components caused by the repair welding procedure [26–28].

Obtaining a thorough image of welding RS distribution using experimental techniques, however, is a daunting task characterized by high prices and labor-intensive procedures. Computational techniques based on the finite element method (FEM), on the other hand, have emerged as powerful tools for determining the complete scope of residual stress distribution within welded joints or structures, drawing considerable attention [29–31]. A FE model was developed to understand the effect of pre-existing stresses on the RS distribution during SUS304 welding. It was found that the initial RSs significantly affected the RSs in the welded pipe away from the heat-affected zone [32–34]. In another study, the RSs were measured in plates using a 3D FEM technique, demonstrating a tri-axial tensile stress structure within the weld and heat-affected zone. In Refs [35–37], RSs were investigated after welding, recommending for the design of repair welds to be as long, narrow, and thin as feasible to reduce RSs in the welded parts. RSs in the welded parts control the mechanical properties, including fatigue life [38].

FEM simulations, on the other hand, are known to be computationally intensive and time-consuming for a given process [39–41]. Recently, various studies have been used to investigate the FEM technique to simulate the various aspects of welding processes [42–44]. Kong et al. [45] developed an FE simulation model to visualize the residual stresses in orthotropic steel deck welding. It was found that the maximum tensile stresses were at the inside and outside weld. In another study by Singh et al. [46], the effect of interlayer was analyzed on microstructure and mechanical properties. The results indicated that the thermal heating and cooling cycles cause a non-uniform cooling rate, altering grain size. Furthermore, the grain dimensions decreased by increasing the interlayer time. Ebrahimi and Hermans [47] proposed a high-fidelity numerical simulation model to explore the effect of various welding configurations on molten pool dynamics in stainless steel sheets. The results show that the non-uniform thermal distribution on the molten surface produces the Marangoni effect, leading to periodic flow oscillations in the molten pool. Similarly, various other studies have also reported the usage of FEM analysis for the manufacturing processes [47–50]. It has been identified that the FEM models require extensive computational resources when scaling up from small to large geometries. One solution is to apply analytical techniques to solve the physics involved in the welding process. The analytical techniques solve mathematical equations directly instead of the meshing technique used in FEM analysis, providing solutions efficiently [51–53]. The solutions provided using analytical techniques are usually provided in closed-loop form, providing a clear understanding of the correlation between the defined variables and system behavior. Besides simulation, various characterization techniques have been explored to identify the RSs in the manufactured parts at the micro-level [54–56].

Recently, arc-based material fusion processes have gained popularity due to the exploration of wire arc-based additive manufacturing (AM) processes. Various experimental studies have been reported in the literature to illustrate the arc-based fusion process. However, very few simulation studies have attempted to explore aspects of the arc-based fusion process. Therefore, efficient simulation models illustrating the multi-physics and complex arc-material interaction phenomena still require attention from the scientific community. To bridge this gap, this study proposes two simulation models: analytical and FEM. In the analytical simulation framework, the thermal history has been calculated using the Goldak heat source and its attenuation due to the simultaneous addition of filler material. This thermal history serves as input to solve the thermal residual stress model using Green's function. For FEM, a thermo-mechanical simulation model has been developed and applied along with the temperature-dependent properties of SUS304. The model has been resolved using a symmetrical approach. Both models have been calibrated using experimental analysis to ensure the trustworthiness of the proposed solution. The proposed model applies to arc welding and arc-based AM processes.

2 Analytical and FEM modeling

This section discusses the analytical and FEM models. For analytical simulation, the heat equation has been solved to estimate thermal distribution for a semi-infinite plate using a bi-ellipsoidal heat equation considering the arc torch attenuation due to the simultaneous addition of filler material. The thermal output is used in the thermal residual stress distribution model solved using Green's function. For FEM analysis, a three-dimensional thermo-mechanical model has been solved utilizing the discretization technique by dividing the continuous domain into smaller elements. FEM involves the iterative process until the solution converges for the defined problem along with the boundary and initial conditions. Analytical solutions are computationally efficient and cost-effective compared to the FEM technique due to the aforementioned reason.

2.1 Analytical model

Figure 1 illustrates the schematic of the arc welding process where a Goldak heat source is joining two base plates with the overall dimensions (LB × WB × HB) along with the addition of a filler material. Such a heating source can be described as a double-ellipsoidal heating source having the

front half as a quarter of one ellipsoid while the rear half is a quarter of a second ellipsoid. Here, LB, WB, and HB are the length, width, and height of the baseplate, and a_{hf}, a_{hb}, f_h, and h_h are the heating source parameters where energy density is equal to 5% referenced to the ellipsoid center. The parameters, including a_{hf}, a_{hb}, f_h, and h_h can be calculated by using the experimental fusion zone.

2.1.1 Thermal distribution

For the arc welding process, the heat equation can be expressed as follows [57]:

$$\lambda\left(\frac{\partial^2 T}{\partial x^2}\right)+\lambda\left(\frac{\partial^2 T}{\partial y^2}\right)+\lambda\left(\frac{\partial^2 T}{\partial z^2}\right)+q_v=\rho C\left(\frac{\partial T}{\partial t}\right). \quad (1)$$

Here, T, λ, q_v, ρ, and C can be designated as thermal distribution, coefficient of heat transfer, inter-heat formation, material's density, and material's specific heat, respectively. For a bi-ellipsoidal heat source moving with time from $t'=0$ to t, the mathematical solution in the case of a semi-infinite plate has been adopted from Ref [58]. After modifications, it is expressed as follows:

$$T=T_o+\frac{3\sqrt{3}\eta_t UI}{\rho C^*\sqrt{\pi}}\int_0^t\left[\frac{dt'}{\sqrt{12\alpha(t-t')+f_h^2}\sqrt{12\alpha(t-t')+h_h^2}}\times\left(\frac{A'}{\sqrt{12\alpha(t-t')+a_{hf}^2}}+\frac{B'}{\sqrt{12\alpha(t-t')+a_{hb}^2}}\right)\right]. \quad (2)$$

$$C^*=\frac{L_f}{T_m-T_o}+C. \quad (3)$$

Here, η_t is the total arc effectiveness; U is the arc voltage; I is the current; ρ is the material density; C^* is the modified heat capacity calculated using enthalpy of fusion (L_f), melting temperature (T_m), room temperature (T_o), and heat capacity of the given material (C); and α is the thermal diffusivity of the material. The terms A' and B' can be calculated as follows [58, 59]:

$$A'=e_f exp\left(-\frac{3(x-vt')^2}{12\alpha(t-t')+f_{hf}^2}-\frac{3y^2}{12\alpha(t-t')+f_h^2}-\frac{3z^2}{12\alpha(t-t')+h_h^2}\right). \quad (4)$$

$$B'=e_b exp\left(-\frac{3(x-vt')^2}{12\alpha(t-t')+f_{hb}^2}-\frac{3y^2}{12\alpha(t-t')+f_h^2}-\frac{3z^2}{12\alpha(t-t')+h_h^2}\right). \quad (5)$$

Here, e_f is the percentage coefficient in the front side of the heating source while e_b is the percentage coefficient in the rear side of the heating source and can be calculated as follows [58, 59]:

$$e_f=\frac{2a_{hf}}{(a_{hf}+a_{hb})}. \quad (6)$$

$$e_b=\frac{2a_{hb}}{(a_{hf}+a_{hb})}. \quad (7)$$

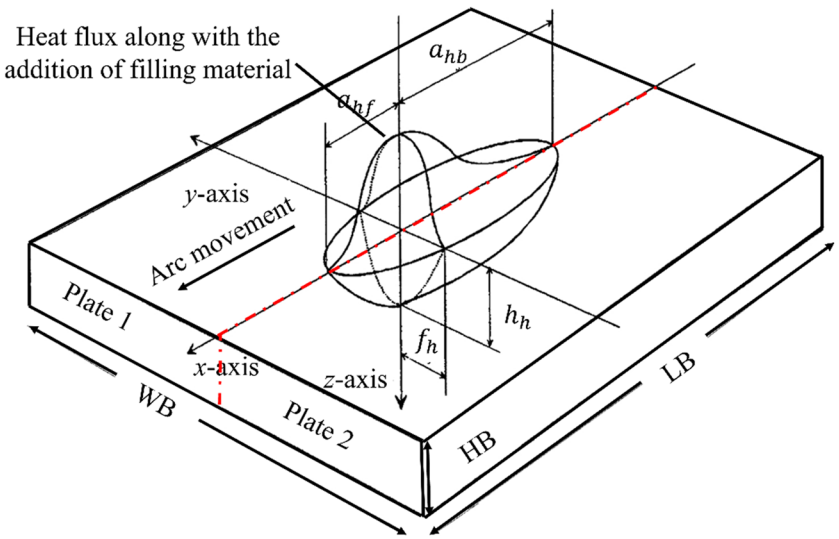

Fig. 1 Schematic of a double-ellipsoid heating source traveling on the joint of two plates and depositing material

During arc welding, a significant proportion of the torch is absorbed by the filler material to change its state from solid to liquid while the rest of the attenuated energy is transmitted to the base plate. As the electrons from the torch fall on a base plate surface, a few of them are absorbed by the plate and generate a melt pool, and the rest of the energy is reflected by the surface. Hence, η_t can be defined as follows:

$$\eta_t = \eta_f + \eta_b, \tag{8}$$

where η_f is the attenuation of the torch energy due to the simultaneous addition of filler material and η_b is the arc torch absorption coefficient by the base plate material. Here, η_b varies from material to material. The η_b can be calculated as follows:

$$\eta_f = \frac{Area\ of\ the\ filler\ material}{Area\ of\ ellipse}. \tag{9}$$

Considering the filler material/wire profile is circular with the radius (r_f), the area of filler material can be calculated as follows:

$$Area\ of\ the\ filler\ material = \pi {r_f}^2. \tag{10}$$

In a double-ellipsoid heating source, the semi-major axis is different for two ellipsoids and calculated as follows:

$$Area\ of\ front\ ellipse = \left(\frac{\pi a_{hf} f_h}{2}\right). \tag{11}$$

$$Area\ of\ rear\ ellipse = \left(\frac{\pi a_{hb} f_h}{2}\right). \tag{12}$$

The final expression for η_f is estimated as follows:

$$\eta_f = \frac{2{r_f}^2}{f_h(a_{hf} + a_{hb})}. \tag{13}$$

The presented model utilizes the material-dependent properties, including heat transfer coefficient, density, specific heat, enthalpy of fusion of a material, and melting temperature of a particular material. Once the abovementioned properties are known, the model can be solved for the particular material. The model can also be tailored for various scanning patterns and geometries by using vector analysis and graph theory, respectively.

2.1.2 Thermal residual stresses

The arc torch involves rapid heating along with slow conduction, resulting in non-uniform thermal distribution, steep temperature gradient, and a variation in the material's thermal expansion coefficient. The aforementioned phenomena are the major causes of thermal residual stresses during arc torch-material interaction [60, 61]. During arc-material interaction, the thermal residual stresses can be calculated using Green's function theorem, normalized stresses, and hydrostatic stresses, if a non-uniform thermal distribution is known, as follows [61, 62]:

$$\sigma_{xx}(x,z) = -\frac{\beta(T)E(T)}{1-2\vartheta(T)}\int_0^{\infty}\int_{-\infty}^{\infty}\left(G_{xh}\frac{\partial T}{\partial x}(x',z') + G_{xv}\frac{\partial T}{\partial z}(x',z')\right)dx'dz' + \frac{2z}{\pi}\int_{-\infty}^{\infty}\frac{p(s)(s-x)^2}{\left((s-x)^2+z^2\right)^2}ds - \frac{\beta(T)E(T)T(x,z)}{1-2\vartheta(T)}. \tag{14}$$

$$\sigma_{zz}(x,z) = -\frac{\beta(T)E(T)}{1-2\vartheta(T)}\int_0^{\infty}\int_{-\infty}^{\infty}\left(G_{zh}\frac{\partial T}{\partial x}(x',z') + G_{zv}\frac{\partial T}{\partial z}(x',z')\right)dx'dz' + \frac{2z^3}{\pi}\int_{-\infty}^{\infty}\frac{p(s)}{\left((s-x)^2+z^2\right)^2}ds - \frac{\beta(T)E(T)T(x,z)}{1-2\vartheta(T)}. \tag{15}$$

$$\sigma_{xz}(x,z) = -\frac{\beta(T)E(T)}{1-2\vartheta(T)}\int_0^{\infty}\int_{-\infty}^{\infty}\left(G_{xzh}\frac{\partial T}{\partial x}(x',z') + G_{xzv}\frac{\partial T}{\partial z}(x',z')\right)dx'dz' + \frac{2z^2}{\pi}\int_{-\infty}^{\infty}\frac{p(s)(s-x)}{\left((s-x)^2+z^2\right)^2}ds. \tag{16}$$

$$\sigma_{yy}(x,z) = \vartheta(T)\left(\sigma_{xx} + \sigma_{zz}\right) - \beta(T)E(T)T(x,z). \tag{17}$$

Here, β, E, and $\partial T/\partial x$ are the thermal expansion, elasticity modulus, and thermal gradient, respectively. Furthermore, $p(s)$ is calculated as follows [61]:

$$p(s) = \frac{\beta(T)E(T)T(x,z=0)}{1-2\vartheta(T)}. \tag{18}$$

Green's function (G_{xh}, G_{xv}, G_{zh}, G_{zv}, G_{xzh}, and G_{xzv}) expressions from Ref [61, 62] have been provided in Appendix A1.

2.2 FEM model

This section discusses the thermal and mechanical models used in this study.

2.2.1 Thermal model

For the arc welding process, the heat equation as defined in Eq. 1 still applies. However, for convenience, it has been rewritten as follows [57]:

$$\lambda\left(\frac{\partial^2 T}{\partial x^2}\right)+\lambda\left(\frac{\partial^2 T}{\partial y^2}\right)+\lambda\left(\frac{\partial^2 T}{\partial z^2}\right)+q_v=\rho C\left(\frac{\partial T}{\partial t}\right). \quad (19)$$

Here, T, λ, q_v, ρ, and C can be designated as thermal distribution, coefficient of heat transfer, inter-heat formation, material's density, and material's specific heat, respectively. The double-ellipsoidal moving heat source was applied for the arc torch. The heat flux density pertaining to the former and latter sections of this heat source model can be elucidated as follows [57]:

$$q_1(x,y,z)=\frac{6\sqrt{3}e_f\eta_t UI}{\pi\sqrt{\pi}c_{hf}h_h f_h}exp\left[-3\left(\frac{x^2}{c_{hf}^2}+\frac{y^2}{{h_h}^2}+\frac{z^2}{{f_h}^2}\right)\right], \quad (20)$$

$$q_2(x,y,z)=\frac{6\sqrt{3}e_b\eta_t UI}{\pi\sqrt{\pi}c_{hb}h_h f_h}exp\left[-3\left(\frac{x^2}{c_{hb}^2}+\frac{y^2}{{h_h}^2}+\frac{z^2}{{f_h}^2}\right)\right], \quad (21)$$

Owing to the dynamic thermal interactions prevailing between the welds and ambient surroundings, the proposed model incorporates two distinctive modes of heat dissipation: (a) convective heat transfer and (b) radiative heat emission, explained using Newton's law of cooling and Stefan-Boltzmann's law, respectively, as follows [57]:

$$q_c=-h_c(T-T_o). \quad (22)$$

$$q_r=-\epsilon_r\sigma_r(T^4-{T_o}^4). \quad (23)$$

Here, h_c, ε, and σ are the coefficient of heat transfer, the material's emissivity, and the Stefan-Boltzmann constant. In the current simulation, the coefficient of heat transfer is 15×10^{-6} W mm^{-2} ℃$^{-1}$, room temperature is set as 20 ℃, and thermal emissivity is 0.8.

2.2.2 Mechanical model

For mechanical analysis, an identical FE model as utilized in the thermal analysis has been employed, with the exception being the variation in element type and boundary conditions. Subsequently, mechanical analysis has been carried out by harnessing the temperature histories obtained from the thermal model as the fundamental input dataset. During the welding process, it is essential to recognize that solid-state phase transformation remains absent in both the base metal and the material to be welded. Hence, the total strain rate (ϵ'_{total}) can be divided into three components [63]:

$$\epsilon'_{total}=\epsilon'_e+\epsilon'_p+\epsilon'_{th}. \quad (24)$$

Here, ϵ'_e, ϵ'_p, and ϵ'_{th} are the elastic, plastic, and thermal strains, respectively. To explain further, the elastic strain is subjected to modeling through the application of isotropic Hook's law, where Young's modulus and Poisson's ratio are both dependent on the prevailing temperature conditions. Concurrently, the thermal strain is determined by using the temperature-dependent coefficient of thermal expansion. To characterize the plastic strain, a rate-independent plastic model has been engaged, incorporating the von Mises yield surface, mechanical properties responsive to variations in temperature, and linear kinematic hardening model [64, 65]. The latter, kinematic hardening, assumes a paramount role due to the inherent tendency of material points to undergo both loading and unloading cycles throughout the intricate welding process [66, 67].

3 Materials and methods

The details of analytical and FEM simulations are provided below. However, for both types of simulations, a customized workstation having AMD Rayzen threadripper 3970X, 16 GB GPU, and 256 GB RAM, was used.

3.1 Experimental calibration

To calibrate the developed analytical and FEM simulation models, the study of Deng and Murakaw [63] was adopted. The authors carried out the welding of SUS304 bulk sheets. The welding was carried out using butt-joint gas tungsten arc (GTA) welding using current = 140 A, voltage = 9.5 V, and speed = 80 mm/min. The terms η_t, e_f, e_b, c_{hf}, c_{hb}, h_h, and f_h have been calculated using experimental fusion zone as 0.7, 1.4, 1.6, 0.002 m, 0.006 m, 0.002 m, and 0.002 m and used for analytical and FEM simulations. The thermocouples were used to measure temperature during the welding process. In the current study, the single-pass experimental analysis was used to calibrate the simulation models initially, and later on, the models were extended to double-pass.

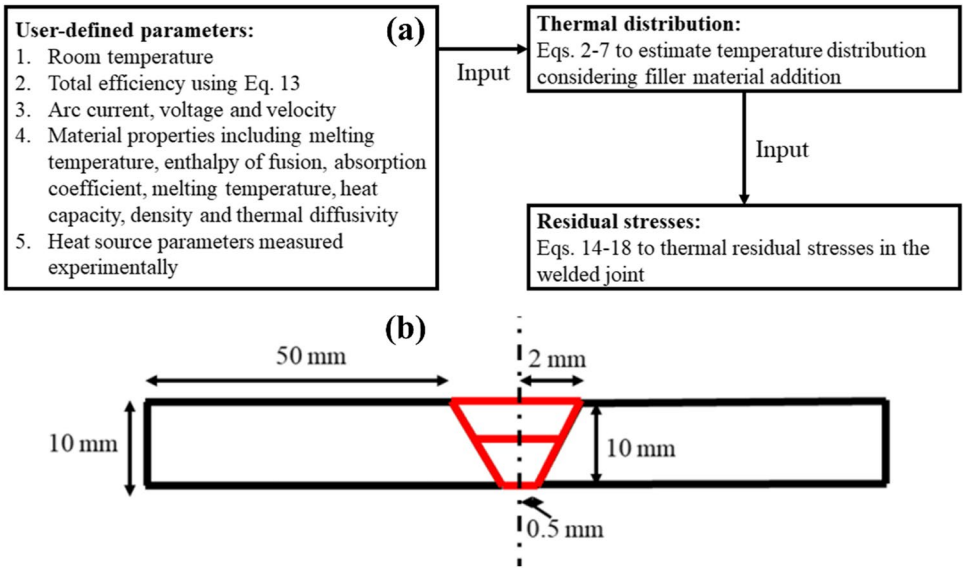

Fig. 2 **a** Analytical simulation framework and **b** schematic of plates to be welded

Table 1 SUS304 material properties used in analytical simulation analysis

Item	Value	Ref.
Melting temperature	1450 ℃	[68]
Enthalpy of fusion	260 J/g	[69]
Heat capacity	502.416 J/kgK	[70]
Density	8.06 Mg/m^3	[71]

3.2 Analytical simulation

For analytical simulations, the framework is presented in Fig. 2a. The parameters, including room temperature, total process efficiency, current, voltage, thermo-physical properties, and heat source experimentally calibrated parameters, were provided as input in Eqs. 2–7 to estimate the thermal distribution along with the filler material. The thermal distribution was used in Eqs. 14–18 to calculate the thermal residual distribution. For welding purposes, SUS304 bulk plates were used. The proposed simulation involves joining two plates, each with dimensions of length = 100 mm, width = 50 mm, and depth = 10 mm, through the application of a two-passes heat source while the length of the weld bead = 100 mm, width of weld bead = 4 mm, and depth of the weld bead = 10 mm. The geometry dimensions are shown in Fig. 2b. These dimensions are different compared to the dimensions used in experimental results. The analytical simulation has been carried out using current = 180 A, voltage = 9.5 V, and speed = 80 mm/min. Furthermore, a cooling time of 300 s was allowed after the welding process.

Table 1 compiles the SUS304 material properties used in the proposed study.

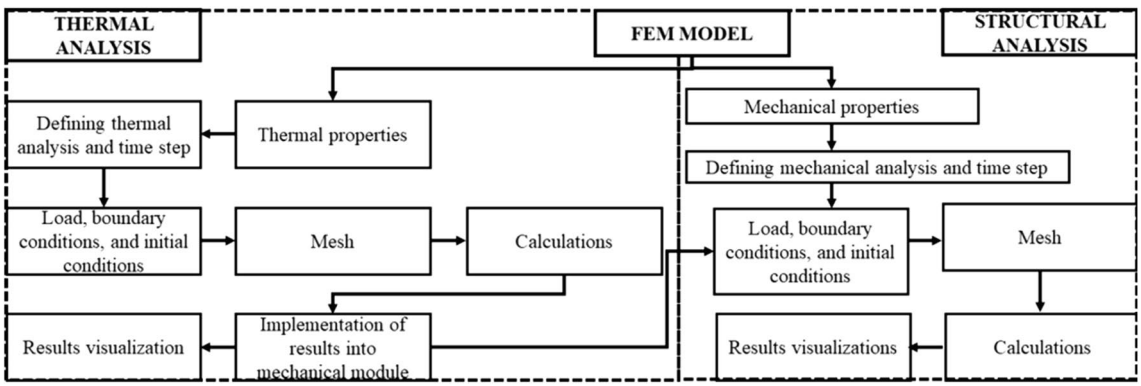

Fig. 3 Schematic of FEM framework

Table 2 SUS304 material properties used in simulation analysis [72]

Temperature (℃)	Heat Capacity ($Jkg^{-1}K^{-1}$)	Conductivity ($Wm^{-1}K^{-1}$)	Density (kg/m^3)	Yield stress (MPa)	Thermal expansion (K^{-1})	Young's modulus (GPa)	Poisson's ratio
0	460	14	790,000	265	1.70	198	0.294
100	490	15.1	788,000	218	1.74	193	0.295
200	510	16	783,000	186	1.80	185	0.301
300	0.52	17	779,000	170	1.86	176	0.310
400	540	18	775,000	155	1.91	167	0.318
600	577	20	766,000	149	1.96	159	0.326
800	600	23	756,000	91	2.02	151	0.333
1200	670	32	737,000	25	2.07	60	0.339
1300	690	33	732,000	21	2.11	20	0.342
1500	700	120	732,000	10	2.10	10	0.338

3.3 FEM simulation

In this section, a sophisticated FEM-based computational approach has been developed and applied using ABAQUS 2020 software to simulate the intricate thermal and mechanical phenomena in SUS304 bulk plates when subjected to arc welding. The simulation captures the temperature fields and resultant thermal residual stresses evolved during the welding process. The FEM framework is shown in Fig. 3, and geometrical dimensions have been elaborated above.

The analysis was divided into two distinct steps. Initially, the heat conduction problem was solved independently, deriving the temporal and spatial distribution of temperatures. Subsequently, in the second step, the obtained temperature history at each node served as the thermal load for the ensuing mechanical analysis, enabling the determination of stress distribution within the weld and bulk plates. To accurately represent the thermal properties of the SUS304, temperature-dependent material properties have been adopted, as summarized in Table 2.

Moreover, the properties of the base plate and material to be welded are identical. The thermal analysis was conducted utilizing the 8-node 3D thermal element DC3D8 with a single degree of freedom, for both base and bead materials. For

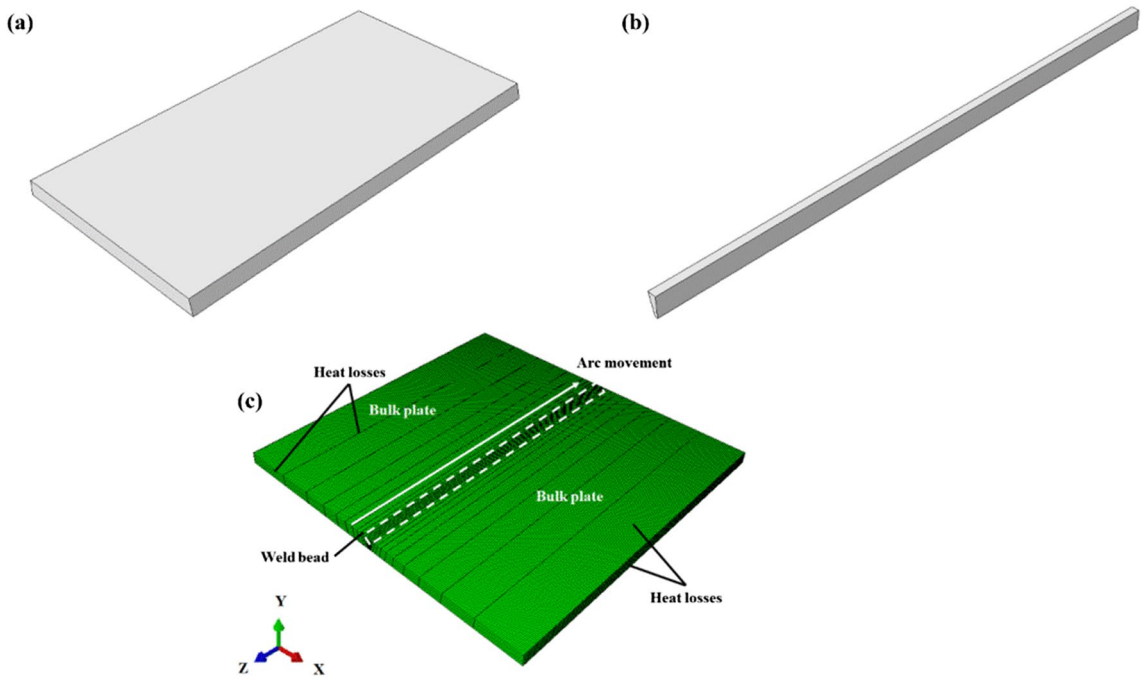

Fig. 4 Arc welding model in ABAQUS software **a** bulk plate, **b** weld bead, and **c** complete model for analysis

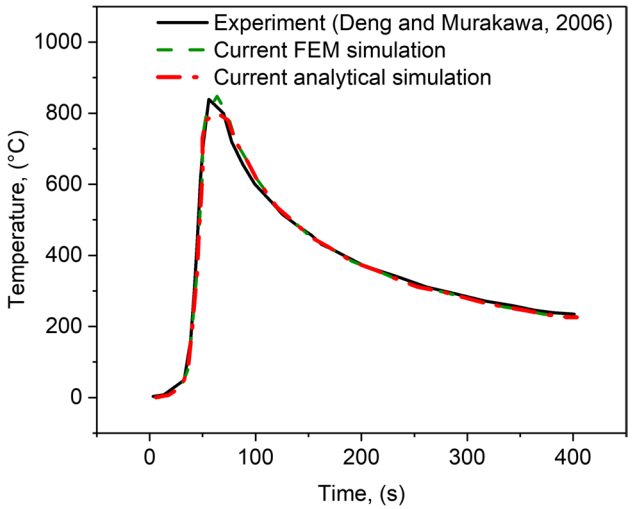

Fig. 5 Comparison of thermal distribution among proposed analytical, FEM simulation, and experiment [63]

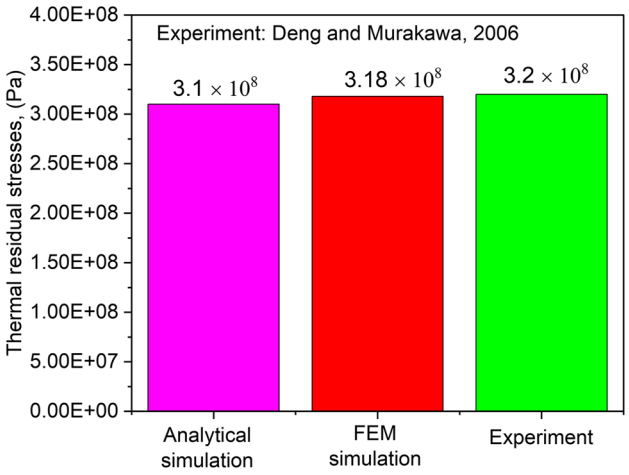

Fig. 6 Comparison of thermal residual stresses among proposed analytical, FEM simulation, and experiment [63]

the mechanical analysis, the solid element type C3D8R, an 8-node bi-quadratic stress/displacement quadrilateral with reduced integration was utilized. To optimize computational efficiency, the model was solved using the "symmetrical" technique. Furthermore, the DLFUX sub-routine was written and applied to run the heat source over the plates to be welded. The filler material was added using the element "birth and death" technique. Figure 4a–c show the bulk plate, weld bead, and final model used for analysis in the ABAQUS software. The FEM simulation has been carried out using current = 180 A, voltage = 9.5 V, and speed = 80 mm/min. A cooling time of 300 s was allowed after the welding process.

Detailed insights for the computational model are provided in Appendix A2.

4 Results and discussions

This section discusses the analytical and FEM model results and their validation with experiments.

4.1 Analytical and FEM simulation model calibration with experimental analysis

For a single pass, a calibration was carried out for the thermal results obtained using the current analytical and FEM simulations with those provided in Ref [63] and are provided in Fig. 5. For analytical and FEM simulations, current = 140 A, voltage = 9.5 V, and speed = 80 mm/min were utilized. In the case of FEM simulation, the results show that both the peak temperature and the cooling rate at the respective location correlate very well with the experimental analyses. However, the peak temperature for analytical simulation presented a noticeable difference concerning the experimental and FEM analyses. It can be explained by the fact that the analytical simulation does not include temperature-dependent material properties that can affect the precision of thermal history.

The calibration results for thermal residual stresses generated using analytical and FEM simulation models as well as experimental analysis [63] are presented in Fig. 6. It can be analyzed that the residual stresses predicted by the FEM as well as analytical models are close to the experimental analysis after calibration. However, it is important to mention here that the FEM simulation took up to ≈ 3.5 h to complete single-track simulation only while the analytical simulation was carried out in ≈ 72 s, saving computational resources and time at the verge of solution precision.

Following the thermal and residual stress distribution models' calibration, the models were extended from a single pass to a double pass. The results are explained below.

4.2 Analytical simulation results

Figure 7a, d show the thermal distribution and melt pool dimensions during the first and second passes at the beginning and end of the arc welding process. The melt pool due to arc-material interaction illustrates that the dimensions are ellipsoid in shape due to the utilization of a Goldak heat source. The provided legends are only applicable to the end of the scan. Furthermore, the solidified, mushy, and liquified zones can be observed within the generated melt pool. In welding, the heat-affected zone (HAZ) and mushy zone are commonly available. HAZ is described as a region in the baseplate surrounded by a weld that experiences the change

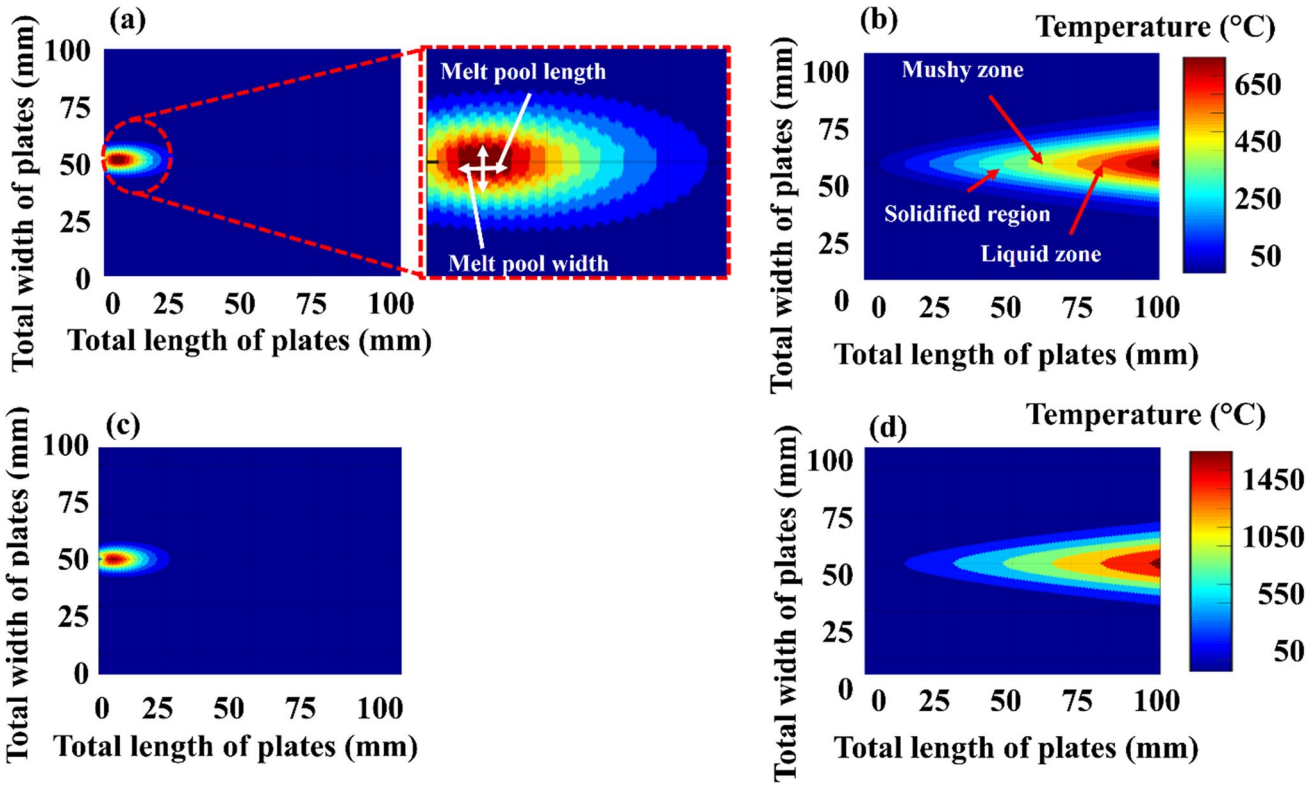

Fig. 7 Thermal distribution at the beginning and end of plates during arc welding: **a, b** first pass and **c, d** second pass; the legend bars show the temperature when the plates have been cooled down

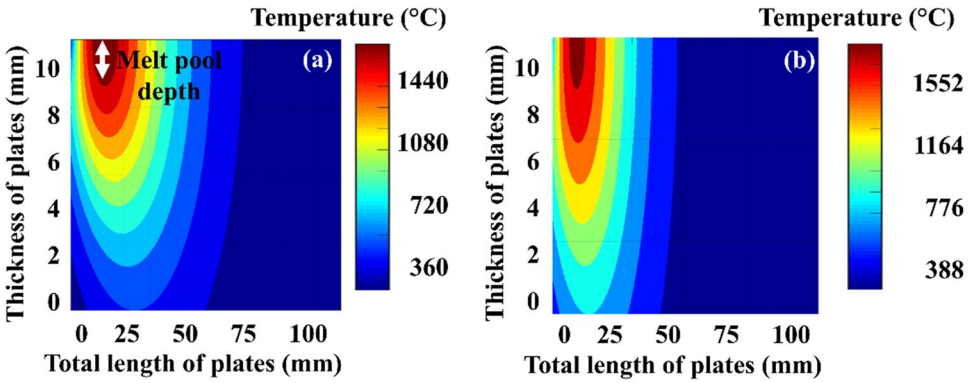

Fig. 8 Thermal distribution across the plates during arc welding: **a** first pass and **b** second pass

in the microstructure due to the heat generated during the welding process while the mushy zone, also designated as the fusion zone or weld bead, is explained by the regime where the baseplate and filler materials have been melted and mixed. After cooling down, the temperature observed during the first pass is around 780 ℃ while it reaches up to 1450 ℃ during the second pass of the arc welding process due to rapid heating and slow conduction involved in the arc welding process.

The melt pool dimensions across the weld plates during the first and second passes of the arc welding process are presented in Fig. 8a, b, respectively, showing the solidified, mushy, and liquified zones. These results are presented when the torch is at the beginning of the plate. It can be identified that the melt pool dimensions during the second pass increased in dimensions due to elevated arc-material interaction time.

In the case of the first and second arc welding processes, the temperature history from the thermal model was utilized as an input to the thermal residual stress distribution model, and results are presented in Fig. 9a, b, respectively. The results have been presented at the top of the deposition along the arc movement direction. During the first pass, it can be analyzed that the thermal distribution was

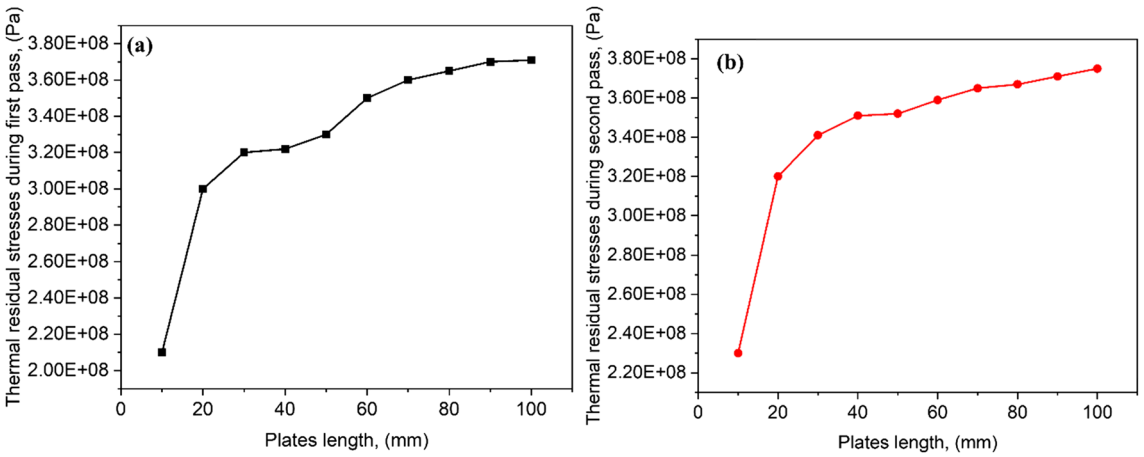

Fig. 9 Thermal residual stresses at the top of the weld bead during arc welding: **a** first pass and **b** second pass

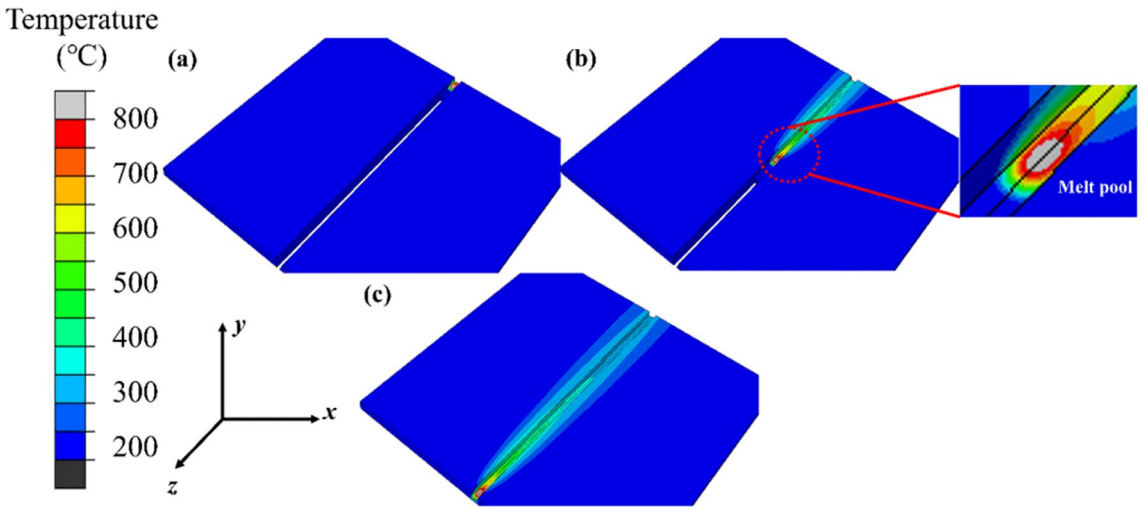

Fig. 10 Thermal distribution during the first pass of welding: **a** beginning, **b** middle, and **c** end of the scan after cooling; the legend bars show the temperature when the plates have been cooled down

calculated within the 2.00×10^8–3.60×10^8 Pa. The last and highest magnitudes were identified at the beginning and end of the plate, respectively. However, during the second weld pass, the thermal residual stresses increased from 2.00×10^8–3.80×10^8 to 2.20×10^8–3.80×10^8 Pa due to enhanced arc-material interaction time, resulting in more heat deposition into the material causing non-uniform thermal gradient. It, in return, increases the thermal residual stresses inside the plates.

4.3 FEM simulation results

Figure 10a–c shows the temperature distribution in the weld as well as the bulk plate during the first pass of the welding process captured using the FEM simulation framework. The utilized parameter resulted in 820 ℃ temperature during the first pass of arc-material interaction after cooling. The provided legend bar applies when the torch is at the end of the scan. To visualize the thermal distribution within the melt pool, a sophisticated multi-color coding scheme has been employed. The melted region has been shown using gray and red color codes, providing valuable insight into the melt pool dimensions as well as the fusion zone.

The simulation results for the second weld pass are shown in Fig. 11a–c. The results show that the peak temperature distribution increased from 820 to 1420 °C while moving from the first to second pass of arc welding after cooling. The provided legend bar applies when the torch is at the end of the scan. In arc welding, this enhancement can be

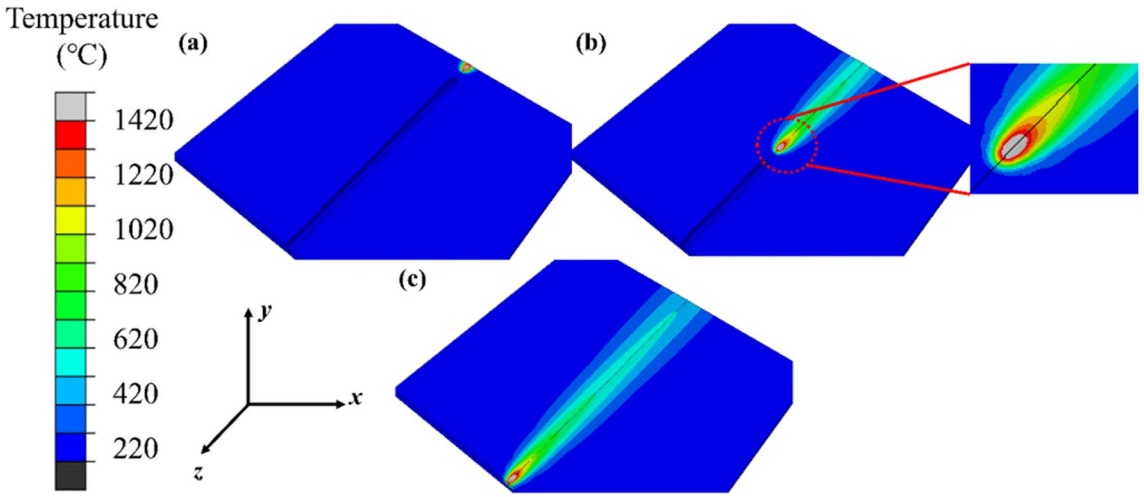

Fig. 11 Thermal distribution during the second pass of welding: **a** beginning, **b** middle, and **c** end of scan after cooling; the legend bars show the temperature when the plates have been cooled down

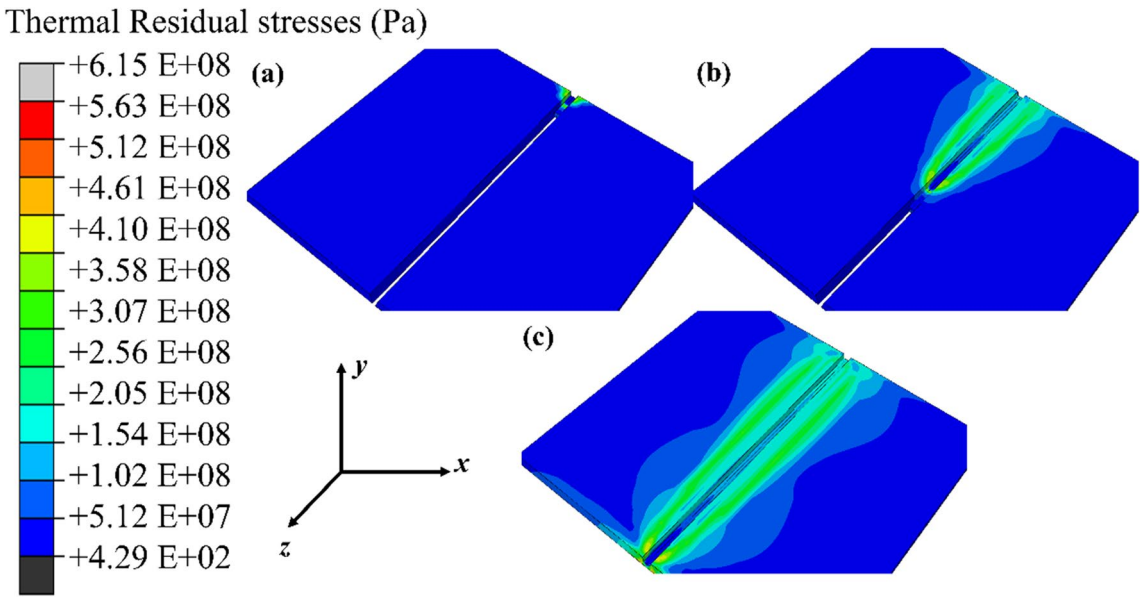

Fig. 12 Residual stress distribution during the first welding pass: **a** beginning, **b** middle, and **c** end of scan after cooling

explained by the rapid heating predominates over slow conduction, resulting in considerable heat entrapment within the weld as well as the base plate. As a result, this phenomenon results in increased heat distribution and melt pool dimensions compared to the first weld pass.

Figure 12a–c depicts the comprehensive thermal residual stress distribution in both the bulk plate and weld bead during the first weld pass. These results are visualized using color-contour representations, offering insights into the stress state of materials subjected to complex loading conditions. Upon analysis, it is evident that within the weld region, thermal residual stress stresses range from 2.05×10^8 to 3.58×10^8 Pa during the initial weld pass. The provided legend bar applies when the torch is at the end of the scan. During arc-material interaction, residual stresses are generated due to thermal gradient (TG) and cooling (CL) mechanisms [51]. The first mechanism, referred to as TG, is attributed to the temperature differential between the heating zone and the adjacent material. The process involves rapid heating with limited heat conduction, leading to the creation of a steep temperature gradient. Consequently, the material's strength experiences an immediate reduction as the temperature rises. The layer beneath the heating zone

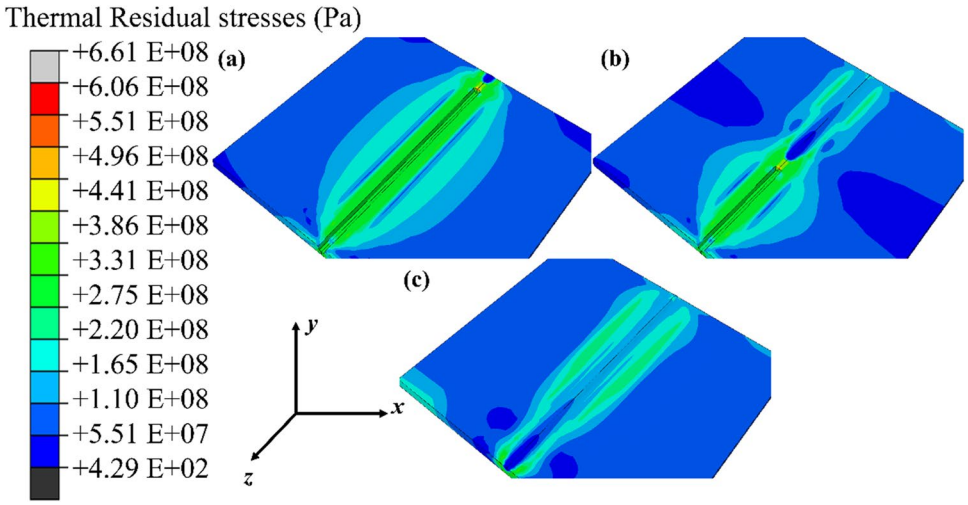

Fig. 13 Residual stress distribution during the second welding pass: **a** beginning, **b** middle, and **c** end of scan after cooling

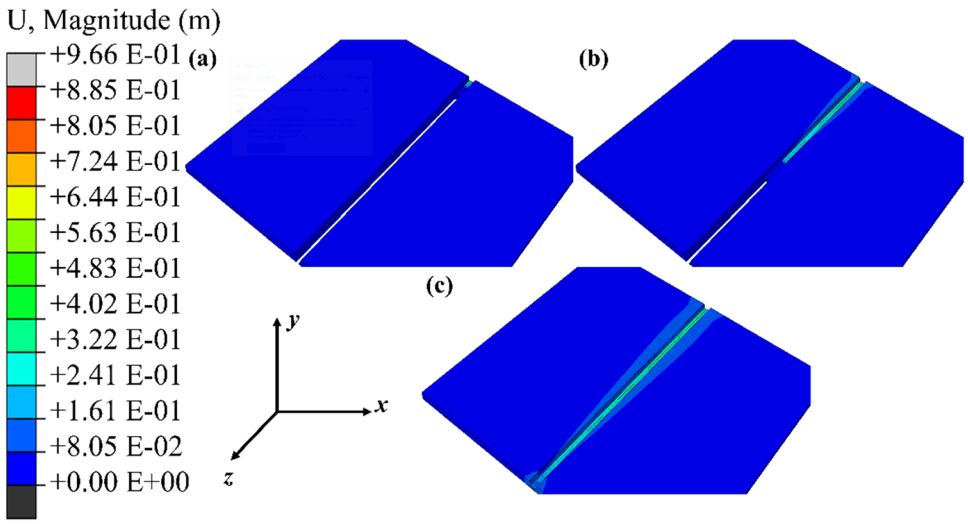

Fig. 14 Deformation during the first welding pass: **a** beginning, **b** middle, and **c** end of scan after cooling

effectively governs the extent of expansion in the heated layer, leading to a compressive stress-strain relationship. In the second mechanism, known as CL, as the welding arc moves away from the previously heated area, the once heated material begins to cool down, resulting in a contraction or shrinkage effect. In response, the underlying material layer opposes these effects, resulting in the development of a tensile stress distribution within the structure.

While moving from the first to the second weld pass, the thermal residual stresses are presented in Fig. 13a, b. The provided legend bar applies when the torch is at the end of the scan. During the second pass, the thermal residual stresses increased from 2.05×10^{8}–3.58×10^{8} to 2.20×10^{8}–3.86×10^{8} Pa. It is due to the elevated arc-material interaction time resulting in enhanced heating and slow conduction.

Figure 14a–c shows the deformation in the bulk plate as well as the weld bead during the first pass, captured using a finite element simulation model. This deformation has been generated due to the induced thermal stresses during arc-welding interaction. A color coding has been applied to identify the resultant deformation arising from the welded regime and distribution in the plates. It can be observed that the maximum deformation during the first pass is equivalent to the $+4.83\times10^{-1}$ m. The legend bar is only applicable when the torch has arrived at the end of the plate. As mentioned above, the TG and CL mechanisms are responsible for the residual

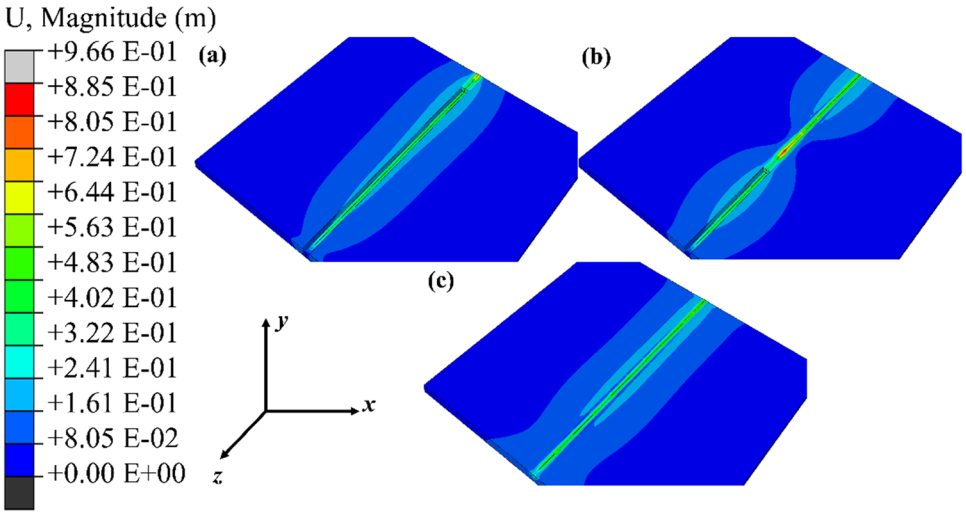

Fig. 15 Deformation during the second welding pass: **a** beginning, **b** middle, and **c** end of scan after cooling

stress induction, leading to the deformation during the first weld pass.

Deformation is presented in Fig. 15a, b while moving from the first to the second pass, monitored using finite element analysis. The provided legend bar applies when the torch is at the end of the scan. During the second pass, the deformation is increased from $+4.83\times10^{-1}$ to $+5.63\times10^{-1}$ m. It is due to the elevated residual stress induction during arc-material interaction.

5 Conclusions and future outlook

5.1 Conclusions

In this study, a comprehensive analysis has been conducted for the thermal and mechanical aspects of the multi-pass arc welding process using analytical and FEM simulations. The developed models were calibrated with experimental data. The investigation was focused on understanding the behavior of the weld bead and surrounding material during both the first and second welding passes. Through the examination of thermal distribution and residual stress, valuable insight has been provided into the complex dynamics of arc-material interaction. For single-layer simulation, the FEM simulation used up to ≈ 3.5 h compared to the analytical model using ≈ 72 s.

One of the key findings of the current study is the significant increinase peak temperature during the second welding pass, which can be attributed to elevated arc-material interaction and the dominance of rapid heating over slow conduction. This phenomenon results in a considerable expansion of the heat-affected zone and melt pool dimensions.

Residual stress analysis revealed the critical role of thermal gradient and cooling mechanisms in generating stress distributions within the weld region. Understanding these stress states is crucial for assessing material strength and predicting componfailuent re.

This research provides a comprehensive understanding of the thermal and mechanical behaviors in arc welding processes. The insights gained from this study can be instrumental in optimizing welding parameters, improving weld quality, and minimizing structural failures in welded components. As welding technology is the ancestor to various additive manufacturing (AM) processes, the proposed simulation can easily be applied to wire arc-based AM (WAAM) processes. The developed simulation steps, conditions, and models apply to WAAM processes.

5.2 Future work

The proposed simulation models offer various benefits for material science, manufacturing, and welding communities, including process parameters before performing the actual experiments. This approach not only saves the experimental resources but also simplifies the process development process. These models can be applied to various metallic materials allowing using their unique thermophysical characteristics. However, these models can be applied to the welding process along a straight line, exhibiting an extent of further improvement. The developed models consider the boundary conditions, including the fixation of plates on all sides (Appendix A2). These models can be further tailored to account for various geometries as well as the boundary conditions such as the weldments mechanically restrained by bolts, pins, or other components within a larger structural framework. This adaptive ability not only highlights the strength of the simulation approach but also permits the exploration of tailored models for specific problem statements.

Appendix A

A1. Analytical model: Green's function solution

The solutions are given below [61, 62].

$$G_{xh} = \frac{1}{4\pi}\frac{1-2\vartheta'}{1-\vartheta'}\left[\frac{3-2\vartheta'}{1-2\vartheta'}\left(\frac{X_m}{X_m^2+Z_p^2}-\frac{X_m}{X_m^2+Z_m^2}\right)+\frac{2}{1-2\vartheta'}\left(\frac{X_m Z_m^2}{\left(X_m^2+Z_m^2\right)^2}-\frac{X_m Z_p^2}{\left(X_m^2+Z_p^2\right)^2}\right)\right]-\frac{1}{\pi}\frac{1}{1-\vartheta'}\times\left(\left(3-2\vartheta'\right)\frac{X_m\left(z'Z_p+X_m^2\right)}{\left(X_m^2+Z_p^2\right)^2}-\frac{3z'^2X_mZ_p^2+X_m^3\left(4z'^2+6zz'+z^2+X_m^2\right)}{\left(X_m^2+Z_p^2\right)^3}\right), \tag{G1}$$

$$G_{zh} = -\frac{1}{4\pi}\frac{1-2\vartheta'}{1-\vartheta'}\left[\left(\frac{X_m}{X_m^2+Z_p^2}-\frac{X_m}{X_m^2+Z_m^2}\right)+\frac{2}{1-2\vartheta'}\left(\frac{X_m Z_m^2}{\left(X_m^2+Z_m^2\right)^2}-\frac{X_m Z_p^2}{\left(X_m^2+Z_p^2\right)^2}\right)\right]-\frac{1}{\pi}\frac{y}{1-\vartheta'}\times\left(\left(3-2\vartheta'\right)\frac{X_m Z_p}{\left(X_m^2+Z_p^2\right)^2}-\frac{X_m\left(4z'^3+9zz'^2+6z^2z'+z^3+zX_m^2\right)}{\left(X_m^2+Z_p^2\right)^3}\right), \tag{G2}$$

$$G_{xzh} = \frac{1}{4\pi}\frac{1-2\vartheta'}{1-\vartheta'}\left[\left(\frac{Z_p}{X_m^2+Z_p^2}-\frac{Z_m}{X_m^2+Z_m^2}\right)+\frac{2}{1-2\vartheta'}\left(\frac{Z_pX_m^2}{\left(X_m^2+Z_p^2\right)^2}-\frac{Z_mX_m^2}{\left(X_m^2+Z_m^2\right)^2}\right)\right]-\frac{1}{\pi}\frac{1}{1-\vartheta'}\times\left(\left(3-2\vartheta'\right)\frac{z'Z_p^2+X_m^2\left(2z+z'\right)}{2\left(X_m^2+Z_p^2\right)^2}-\frac{z'^3\left(z'^2+3zz'^2+3z^2\right)+z^3z'^2+X_m^2\left(z^3+6zz'^2+6z^2z'+z^3\right)+zX_m^4}{\left(X_m^2+Z_p^2\right)^3}\right), \tag{G3}$$

$$G_{xv} = -\frac{1}{4\pi}\frac{1-2\vartheta'}{1-\vartheta'}\left[\left(\frac{Z_p}{X_m^2+Z_p^2}-\frac{Z_m}{X_m^2+Z_m^2}\right)+\frac{2}{1-2\vartheta'}\left(\frac{Z_mX_m^2}{\left(X_m^2+Z_m^2\right)^2}-\frac{Z_pX_m^2}{\left(X_m^2+Z_p^2\right)^2}\right)\right]-\frac{1}{2\pi}\frac{1}{1-\vartheta'}\times\left(2\left(1-\vartheta'\right)\frac{Z_p}{\left(X_m^2+Z_p^2\right)^2}-\frac{\left[2\left(1-\vartheta'\right)z-z'\right]\left(Z_p^2-X_m^2\right)}{\left(X_m^2+Z_p^2\right)^3}+\frac{2zz'Z_p\left(3X_m^2-Z_p^2\right)}{\left(X_m^2+Z_p^2\right)^3}\right), \tag{G4}$$

$$G_{zv} = \frac{1}{4\pi}\frac{1}{1-\vartheta'}\left[\left(3-2\vartheta'\right)\left(\frac{Z_p}{X_m^2+Z_p^2}-\frac{Z_m}{X_m^2+Z_m^2}\right)+2\left(\frac{Z_mX_m^2}{\left(X_m^2+Z_m^2\right)^2}-\frac{Z_pX_m^2}{\left(X_m^2+Z_p^2\right)^2}\right)\right]-\frac{1}{2\pi}\frac{1}{1-\vartheta'}\times\left(2\left(1-\vartheta'\right)\frac{Z_p}{X_m^2+Z_p^2}-\frac{\left[2\left(1-\vartheta'\right)z+z'\right]\left(Z_p^2-X_m^2\right)}{\left(X_m^2+Z_p^2\right)^2}+\frac{2zz'Z_p\left(3X_m^2-Z_p^2\right)}{\left(X_m^2+Z_p^2\right)^3}\right), \tag{G5}$$

$$G_{xzv} = \frac{X_m}{4\pi}\frac{1-2\vartheta'}{1-\vartheta'}\left[\left(\frac{1}{X_m^2+Z_p^2}-\frac{1}{X_m^2+Z_m^2}\right)+\frac{2}{1-2\vartheta'}\left(\frac{Z_p^2}{\left(X_m^2+Z_p^2\right)^2}-\frac{Z_m^2}{\left(X_m^2+Z_m^2\right)^2}\right)\right]-\frac{X_m}{2\pi}\frac{1}{1-\vartheta'}\times\left(4\left(1-\vartheta'\right)\frac{zZ_p}{\left(X_m^2+Z_p^2\right)^2}+\frac{2zz'Z_p\left(3Z_p^2-X_m^2\right)}{\left(X_m^2+Z_p^2\right)^3}\right), \tag{G6}$$

$$X_m = x - x' \tag{G7}$$

$$Z_p = z + z' \tag{G8}$$

$$Z_m = z + z' \tag{G9}$$

Here, x' and z' are the coordinates along the x- and z-directions at which point the heat source acts on the body.

A2. FEM model

The double-pass weld problem has been resolved using the "Symmetrical" technique via ABAUQS 2020 software. Figure 16 explains the steps carried out to develop the FEM model for double-pass arc welding.

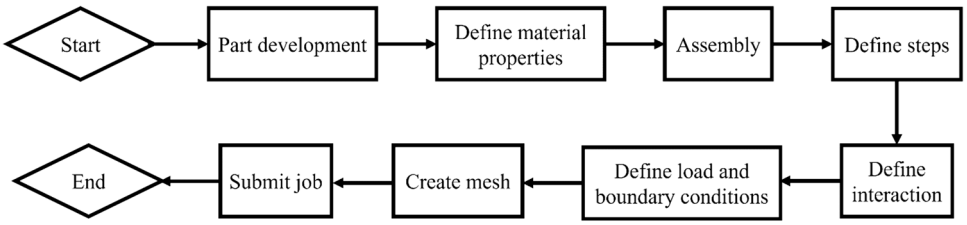

Fig. 16 Schematic to run a simulation analysis in ABAQUS software

A.2.1. Part development

This step involves the generation of bulk plates to be welded as well as welded beads. For this purpose, "3D" and "deformable" options were selected under "modeling space" and "type," respectively, in ABAQUS software. The dimensions of the bulk plate are length = 100 mm, width = 5 mm, and depth = 10 mm, as well as the length of the weld bead = 100 mm, width of weld bead = 4 mm, and depth of the weld bead = 10 mm.

A.2.2. Define material properties

In this step, the properties defined in Table 2 were applied on bulk plates as well as the weld beads. It is important to mention here that the temperature-dependent properties were used here.

A.2.3. Assembly

Here, the bulk plate and weld beads were fused using the "create instance command" while the "instance type" was selected as "dependent (mesh on part)." After creating an assembly, it was divided into two halves, along with the *y*-axis, to satisfy the double-pass weld problem. Following on, a "datum coordinate system" was defined at the beginning as well as at the top of the first pass. This datum coordinate system will serve as a basis to run the heat source (torch) on the material to be welded. After this, a total of nine equally spaced "datum planes" were defined to create partition cells. These partition cells will be used to implement "element birth and death" techniques.

A.2.4. Define steps

In this step, the analysis type was defined. The current simulation model utilizes a coupled thermo-mechanical model to analyze temperature distribution as well as residual stresses and displacement. For this purpose, "coupled temp-displacement (transient)" was selected and applied during the material removal and addition. In the beginning, all the weld beads were deactivated using the "element death" technique. For 1st weld pass, a chunk of material was added using the "element birth" technique. All the elements were generated gradually with respect to time. At the end of the first welding, the cooling step was implied.

A.2.5. Define interaction

Here, the material sections created in A.2.4. were used to apply elements birth and death technique, implemented using "model change" under "interaction manager." Initially, the whole weld bead was deactivated (element death). Following on, the section of the material was activated (element birth) when the strain was applied to the elements. For cooling, "surface film condition" was applied on the bulk plate. Furthermore, to include radiation during the irradiation process, the "surface radiation" was selected and emissivity was defined in the model. Here, "film coefficient, sink temperature, and emissivity" are provided by the user.

A.2.6. Define load and boundary conditions

In this step, the boundary conditions were applied. For boundary condition 1, the initial step was selected with the "mechanical" category with "symmetry/antisymmetry/encastre." The side face of weld beads was chosen, and "XCYMM (U1=UR1=UR3=0)" was used, restricting movement along the *x*-axis and rotation along the *y*- and *z*-axes. Furthermore, the side of the bulk plate having no weld bead was chosen and fixed using "ENCASTRE (U1 = U2 = U3 = UR1 = UR2 = UR3 = 0) boundary condition 2. Following on, "Pre-defined field" was applied on the initial step by selecting "Temperature" under "other" category. Here, the magnitude will be provided as an input to the model. This step provides the starting or room temperature for the developed model. To incorporate the user-defined DFLUX sub-routine, the thermal load was defined under user-defined "Body heat flux." The body heat flux was deactivated at the cooling stage.

A.2.7. Create mesh

In this step, the model was meshed using an approximate global size equivalent to 0.001 m. During analysis, the "coupled temperature-displacement" family type was applied.

A.2.8. Submit the job

Before submitting the job, the model attributes were defined, including absolute zero temperature and Stefan-Boltzmann constant equal to -237.15 ℃ and 5.669×10^{-8} W/m^{2}K^4. After completing the pre-processing, the model was submitted, and the DFLUX sub-routine was submitted for user-defined body heat flux.

Author contribution **Muhammad Arif Mahmood**: conceptualization, data curation, formal analysis, investigation, methodology, visualization, validation, software, writing—original draft, and writing—review and editing. **Usman Tariq**: data curation, formal analysis, investigation, resources, validation, visualization, writing—original draft, and writing – review and editing. **Mihai Oane**: data curation, investigation, methodology, validation, visualization, writing—original draft, and writing—review and editing. **Frank Liou**: visualization, writing—review and editing, supervision, and funding acquisition. All authors have read and agreed to the published version of the manuscript.

Funding This research was supported by the National Science Foundation Grants CMMI-1625736 and EEC 1937128 and the Intelligent Systems Center at Missouri S&T.

Data availability Not applicable.

Declarations

Ethical approval Not applicable.

Consent to participate Not applicable.

Consent to publish Not applicable.

Conflict of interest The authors declare no competing interests.

References

1. Féron D (2012) Overview of nuclear materials and nuclear corrosion science and engineering. Nucl Corros Sci Eng 31–56. https://doi.org/10.1533/9780857095343.1.31
2. Mahmoudinezhad S, Sadi M, Ghiasirad H, Arabkoohsar A (2023) A comprehensive review on the current technologies and recent developments in high-temperature heat exchangers. Renew Sustain Energy Rev 183:113467. https://doi.org/10.1016/J.RSER.2023.113467
3. Cavallo C (2023) 304 stainless steel (properties, strength, and uses). https://www.thomasnet.com/articles/metals-metal-products/all-about-304-steel-properties-strength-and-uses/. Accessed 22 Mar 2024
4. Terrani KA, Zinkle SJ, Snead LL (2014) Advanced oxidation-resistant iron-based alloys for LWR fuel cladding. J Nucl Mater 448:420–435. https://doi.org/10.1016/J.JNUCMAT.2013.06.041
5. Fang JX, Wang JX, Wang YJ et al (2022) Microstructure evolution and deformation behavior during stretching of a compositionally inhomogeneous TWIP-TRIP cantor-like alloy by laser powder deposition. Mater Sci Eng A 847:143319. https://doi.org/10.1016/J.MSEA.2022.143319
6. Jiang YL, Fang JX, Ma GZ et al (2021) Microstructure and properties of an as-deposited and post treated high strength carbide-free bainite steel fabricated via laser powder deposition. Mater Sci Eng A 824:141791. https://doi.org/10.1016/J.MSEA.2021.141791
7. Sazonova SA, Nikolenko SD, Osipov AA et al (2021) Weld defects and automation of methods for their detection. J Phys Conf Ser 1889:022078. https://doi.org/10.1088/1742-6596/1889/2/022078
8. Zhang S, Zhang S, Zhou H et al (2024) Preparation and characterization of Sn-3.0Ag-0.5Cu nano-solder paste and assessment of the reliability of joints fabricated by microwave hybrid heating. Mater Charact 207:113512. https://doi.org/10.1016/J.MATCHAR.2023.113512
9. Wang J, Pan Z, Wang Y et al (2020) Evolution of crystallographic orientation, precipitation, phase transformation and mechanical properties realized by enhancing deposition current for dual-wire arc additive manufactured Ni-rich NiTi alloy. Addit Manuf 34:101240. https://doi.org/10.1016/J.ADDMA.2020.101240
10. Silva GC, de Castro JA, Filho RMM et al (2019) Comparing two different arc welding processes through the welding energy: a selection analysis based on quality and energy consumption. J Brazilian Soc Mech Sci Eng 41:1–12. https://doi.org/10.1007/S40430-019-1804-X/METRICS
11. Fang JX, Li SB, Dong SY et al (2019) Effects of phase transition temperature and preheating on residual stress in multi-pass & multi-layer laser metal deposition. J Alloys Compd 792:928–937. https://doi.org/10.1016/J.JALLCOM.2019.04.104
12. Xu S, Jing X, Zhu P et al (2023) Equilibrium phase diagram design and structural optimization of SAC/Sn-Pb composite structure solder joint for preferable stress distribution. Mater Charact 206:113389. https://doi.org/10.1016/J.MATCHAR.2023.113389
13. Tariq U, Joy R, Wu S-H et al (2023) A state-of-the-art digital factory integrating digital twin for laser additive and subtractive manufacturing processes. https://doi.org/10.1108/RPJ-03-2023-0113. Rapid Prototyp J ahead-of-print
14. Song J, Chen Y, Hao X et al (2024) Microstructure and mechanical properties of novel Ni–Cr–Co-based superalloy GTAW joints. J Mater Res Technol 29:2758–2767. https://doi.org/10.1016/J.JMRT.2024.01.241
15. Singh G, Saxena RK, Pandey S (2021) Investigating the effect of arc offsetting in AISI 304 stainless steel and copper welding using gas tungsten arc welding. J Brazilian Soc Mech Sci Eng 43:1–22. https://doi.org/10.1007/S40430-021-02877-X/METRICS
16. Karpagaraj A, Rajesh Kumar N, Thiyaneshwaran N et al (2020) Experimental and numerical studies on gas tungsten arc welding of Ti–6Al–4V tailor-welded blank. J Brazilian Soc Mech Sci Eng 42:1–11. https://doi.org/10.1007/S40430-020-02629-3/METRICS
17. Jandaghi MR, Pouraliakbar H, Iannucci L et al (2023) Comparative assessment of gas and water atomized powders for additive manufacturing of 316 L stainless steel: microstructure, mechanical properties, and corrosion resistance. Mater Charact 204:113204. https://doi.org/10.1016/J.MATCHAR.2023.113204
18. Jandaghi MR, Pouraliakbar H, Shim SH et al (2022) In-situ alloying of stainless steel 316L by co-inoculation of Ti and Mn using LPBF additive manufacturing: Microstructural evolution and mechanical properties. Mater Sci Eng A 857:144114. https://doi.org/10.1016/J.MSEA.2022.144114
19. Jandaghi MR, Saboori A, Iuliano L, Pavese M (2021) On the effect of rapid annealing on the microstructure and mechanical behavior of additively manufactured stainless steel by laser powder bed fusion. Mater Sci Eng A 828:142109. https://doi.org/10.1016/J.MSEA.2021.142109
20. Chen F, Zhang H, Li Z et al (2023) Residual stresses effects on fatigue crack growth behavior of rib-to-deck double-sided welded joints in orthotropic steel decks. https://doi org/101177/13694332231213462 27:35–50. https://doi.org/10.1177/13694332231213462
21. Jiang XJ, Bao SJ, Zhang LW et al (2023) Effect of zr on microstructure and properties of TC4 alloy fabricated by laser additive manufacturing. J Mater Res Technol 24:8782–8792. https://doi.org/10.1016/J.JMRT.2023.05.137
22. Long X, Su T, Lu C et al (2023) An insight into dynamic properties of SAC305 lead-free solder under high strain rates and high temperatures. Int J Impact Eng 175:104542. https://doi.org/10.1016/J.IJIMPENG.2023.104542
23. Kim JH, Ballinger RG (2008) Stress corrosion cracking crack growth behavior of type 316L stainless steel weld metals in boiling water reactor environments. Corrosion 64:645–656. https://doi.org/10.5006/1.3279925
24. Iwamatsu F, Miyazaki K, Mochizuki M (2013) Estimation of SCC crack growth behavior under weld residual stress in the bottom of a reactor pressure vessel by finite element analysis. Am Soc Mech Eng Press Vessel Pip Div PVP 6:703–709. https://doi.org/10.1115/PVP2012-78471
25. Lu Z, Shoji T, Takeda Y et al (2008) Effects of loading mode and water chemistry on stress corrosion crack growth behavior of 316L HAZ and weld metal materials in high temperature pure water. Corros Sci 50:625–638. https://doi.org/10.1016/J.CORSCI.2007.08.021
26. Xie J, Zhou Y, Zhou C et al (2024) Microstructure and mechanical properties of Mg–Li alloys fabricated by wire arc additive manufacturing. J Mater Res Technol 29:3487–3493. https://doi.org/10.1016/J.JMRT.2024.02.094
27. Long X, Lu C, Su Y, Dai Y (2023) Machine learning framework for predicting the low cycle fatigue life of lead-free solders. Eng Fail Anal 148:107228. https://doi.org/10.1016/J.ENGFAILANAL.2023.107228
28. Xie J, Chen Y, Wang H et al (2024) Phase transformation mechanisms of NiTi shape memory alloy during electromagnetic

pulse welding of Al/NiTi dissimilar joints. Mater Sci Eng A 893:146119. https://doi.org/10.1016/J.MSEA.2024.146119
29. Zhang H, Zhang L, Liu Z et al (2021) Numerical analysis of hybrid (bonded/bolted) FRP composite joints: a review. Compos Struct 262:113606. https://doi.org/10.1016/J.COMPSTRUCT.2021.113606
30. Prabhakar DAP, Shettigar AK, Herbert MA et al (2022) A comprehensive review of friction stir techniques in structural materials and alloys: challenges and trends. J Mater Res Technol 20:3025–3060. https://doi.org/10.1016/J.JMRT.2022.08.034
31. Threadgilll PL, Leonard AJ, Shercliff HR, Withers PJ (2009) Friction stir welding of aluminium alloys. Int Mater Rev 54:49–93. https://doi.org/10.1179/174328009X411136
32. Yang Z, Tang B, Qiu Y et al (2023) Measurement of transient temperature using laser-induced breakdown spectroscopy (LIBS) with the surface temperature effect. J Anal Spectrom 38:1952–1961. https://doi.org/10.1039/D3JA00128H
33. Wu Y, Chen J, Zhang L et al (2022) Effect of boron on the structural stability, mechanical properties, and electronic structures of γ′-Ni3Al in TLP joints of nickel-based single-crystal alloys. Mater Today Commun 31:103375. https://doi.org/10.1016/J.MTCOMM.2022.103375
34. Gao Q, Ding Z, Liao WH (2022) Effective elastic properties of irregular auxetic structures. Compos Struct 287:115269. https://doi.org/10.1016/J.COMPSTRUCT.2022.115269
35. Dong P, Zhang J, Bouchard PJ (2002) Effects of repair weld length on residual stress distribution. J Press Vessel Technol 124:74–80. https://doi.org/10.1115/1.1429230
36. Song S, Dong P (2017) Residual stresses at weld repairs and effects of repair geometry. Sci Technol Weld Join 22:265–277. https://doi.org/10.1080/13621718.2016.1224544
37. Dong P, Hong JK, Bouchard PJ (2005) Analysis of residual stresses at weld repairs. Int J Press Vessel Pip 82:258–269. https://doi.org/10.1016/J.IJPVP.2004.08.004
38. Hu JC, Yang K, Wang QY et al (2024) Ultra-long life fatigue behavior of a high-entropy alloy. Int J Fatigue 178:108013. https://doi.org/10.1016/J.IJFATIGUE.2023.108013
39. Wang H, Wang F, Qian D et al (2023) Investigation of damage mechanisms related to microstructural features of ferrite-cementite steels via experiments and multiscale simulations. Int J Plast 170:103745. https://doi.org/10.1016/J.IJPLAS.2023.103745
40. Hua L, Liu Y, Qian D et al (2022) Mechanism of void healing in cold rolled aeroengine M50 bearing steel under electroshocking treatment: a combined experimental and simulation study. Mater Charact 185:111736. https://doi.org/10.1016/J.MATCHAR.2022.111736
41. Zhou J, Qi Q, Liu Q et al (2024) Determining residual stress profile induced by end milling from measured thin plate deformation. Thin-Walled Struct 200:111862. https://doi.org/10.1016/J.TWS.2024.111862
42. Zhang Z, Chen J, Wang J et al (2022) Effects of solder thickness on interface behavior and nanoindentation characteristics in Cu/Sn/Cu microbumps. Weld World 66:973–983. https://doi.org/10.1007/S40194-022-01261-0
43. Luo Y, Liu X, Chen F et al (2023) Numerical simulation on crack–inclusion interaction for rib-to-deck welded joints in orthotropic steel deck. Met 13:1402. https://doi.org/10.3390/MET13081402
44. Gong Z, Zhang T, Chen Y et al (2024) Effect of laser shock peening on stress corrosion cracking of TC4/2A14 dissimilar metal friction stir welding joints. J Mater Res Technol 30:1716–1725. https://doi.org/10.1016/J.JMRT.2024.03.216
45. Kong W, Huang W, Wei Y (2024) Numerical study on welding residual stress by double-sided submerged arc welding for orthotropic steel deck. Eng Struct 302:117445. https://doi.org/10.1016/J.ENGSTRUCT.2024.117445
46. Singh A, Kumar V, Mandal A (2024) An experimental and numerical study on the influence of interlayer time interval in wire-arc additive manufacturing process. Proceedings of the Institution of Mechanical Engineers, Part C: Journal of Mechanical Engineering Science 0(0). https://doi.org/10.1177/09544062241233490
47. Ebrahimi A, Hermans MJM (2023) Laser butt welding of thin stainless steel 316L sheets in asymmetric configurations: a numerical study. J Adv Join Process 8:100154. https://doi.org/10.1016/J.JAJP.2023.100154
48. Skejić D, Žuvelek V, Valčić A (2023) Parametric numerical study of welded aluminium beam-to-column joints. Build 13:718. https://doi.org/10.3390/BUILDINGS13030718
49. Tajik N, Mirghaderi SR, Asghari A, Hamidia M (2024) Experimental and numerical study on weld strengths of built-up steel box columns. J Constr Steel Res 213:108362. https://doi.org/10.1016/J.JCSR.2023.108362
50. Cao X, Wang H, Chen Y et al (2023) Experimental and numerical study of residual stresses in 550 MPa high strength steel welded angle sections. Structures 56:104907. https://doi.org/10.1016/J.ISTRUC.2023.104907
51. Mahmood MA, Popescu AC, Hapenciuc CL et al (2020) Estimation of clad geometry and corresponding residual stress distribution in laser melting deposition: analytical modeling and experimental correlations. Int J Adv Manuf Technol 111:77–91. https://doi.org/10.1007/S00170-020-06047-6
52. Guo H, Zhang J (2023) Expansion of sandwich tubes with metal foam core under axial compression. J Appl Mech Trans ASME 90. https://doi.org/10.1115/1.4056686
53. Shi J, Zhao B, Tu L et al (2024) Transient lubrication analysis of journal-thrust coupled bearing considering time-varying loads and thermal-pressure coupled effect. Tribol Int 194:109502. https://doi.org/10.1016/J.TRIBOINT.2024.109502
54. Wu Y, Deng B, Li X et al (2024) In-situ EBSD study on twinning activity caused by deep cryogenic treatment (DCT) for an as-cast AZ31 mg alloy. J Mater Res Technol 30:3840–3850. https://doi.org/10.1016/J.JMRT.2024.04.099
55. Li W, Liu H, Zhu J et al (2024) Efficient photocathodic protection of nanoflower MgIn2S4-modified CNNs composites on 316 SS under visible light. Mater Res Bull 173:112694. https://doi.org/10.1016/J.MATERRESBULL.2024.112694
56. Gong Q, Cai M, Gong Y et al (2024) Grinding surface and subsurface stress load of nickel-based single crystal superalloy DD5. Precis Eng 88:354–366. https://doi.org/10.1016/J.PRECISIONENG.2024.02.017
57. Dai P, Wang Y, Li S et al (2020) FEM analysis of residual stress induced by repair welding in SUS304 stainless steel pipe butt-welded joint. J Manuf Process 58:975–983. https://doi.org/10.1016/j.jmapro.2020.09.006
58. Nguyen NT, Ohta A, Matsuoka K et al (1999) Analytical solutions for transient temperature of semi-infinite body subjected to 3-D moving heat sources. Weld J (Miami, Fla) 78:265-s-274-s
59. Goyal VK, Ghosh PK, Saini JS (2009) Analytical studies on thermal behaviour and geometry of weld pool in pulsed current gas metal arc welding. J Mater Process Technol 209:1318–1336. https://doi.org/10.1016/J.JMATPROTEC.2008.03.035
60. Woo W, Kim DK, Kingston EJ et al (2019) Effect of interlayers and scanning strategies on through-thickness residual stress distributions in additive manufactured ferritic-austenitic steel structure. Mater Sci Eng A 744:618–629. https://doi.org/10.1016/J.MSEA.2018.12.078
61. Mirkoohi E, Li D, Garmestani H, Liang SY (2021) Residual stress modeling considering microstructure evolution in metal additive manufacturing. J Manuf Process 68:383–397. https://doi.org/10.1016/J.JMAPRO.2021.04.041
62. Saif MTA, Hui CY, Zehnder AT (1993) Interface shear stresses induced by non-uniform heating of a film on a substrate. Thin

Solid Films 224:159–167. https://doi.org/10.1016/0040-6090(93)90427-Q
63. Deng D, Murakawa H (2006) Numerical simulation of temperature field and residual stress in multi-pass welds in stainless steel pipe and comparison with experimental measurements. Comput Mater Sci 37:269–277. https://doi.org/10.1016/j.commatsci.2005.07.007
64. Zhu Q, Chen J, Gou G et al (2017) Ameliorated longitudinal critically refracted—attenuation velocity method for welding residual stress measurement. J Mater Process Technol 246:267–275. https://doi.org/10.1016/J.JMATPROTEC.2017.03.022
65. Gan M, Chong X, Lu T et al (2024) Unveiling thermal stresses in RETaO4 (RE = nd, Sm, Eu, Gd, Tb, Dy, Ho and Er) by first-principles calculations and finite element simulations. Acta Mater 271:119904. https://doi.org/10.1016/J.ACTAMAT.2024.119904
66. Manai A, Manai A (2021) Residual stresses distribution posterior to welding and cutting processes. https://doi.org/10.5772/INTECHOPEN.100610. Eng Princ - Weld Residual Stress
67. Guo Q, Hou H, Wang K et al (2023) Coalescence of Al0.3CoCrFeNi polycrystalline high-entropy alloy in hot-pressed sintering: a molecular dynamics and phase-field study. Npj Comput Mater 2023 91 9:1–13. https://doi.org/10.1038/s41524-023-01139-9
68. Material WM point of stainless steel 304. https://www.theworldmaterial.com/melting-point-of-stainless-steel/. Accessed 9 Nov 2023
69. Yamaguchi K, Ueda S (2012) High temperature enthalpy measurement of SUS340 stainless steel. High Temp Mater Process 30:569–572. https://doi.org/10.1515/HTMP.2011.115/MACHINEREADABLECITATION/RIS
70. Edge E Specific heat capacity of metals table chart https://www.engineersedge.com/materials/specific_heat_capacity_of_metals_13259.htm. Accessed 9 Nov 2023
71. Stainless steel materials A - grade 304. https://www.azom.com/properties.aspx?ArticleID=965. Accessed 11 Sep 2023
72. Feli S, Aaleagha MEA, Jahanban MR (2017) Evaluation effects of modeling parameters on the temperature fields and residual stresses of butt-welded stainless steel pipes. Journal of Stress Analysis 1(2):25–33